Variability of Ventricular Repolarization Dispersion Quantified by Time-Warping the Morphology of the T-Waves

Julia Ramírez*, Michele Orini, J. Derek Tucker, Esther Pueyo, and Pablo Laguna

Abstract*—*Objective: **We propose two electrocardiogram (ECG)-derived markers of T-wave morphological variability in the temporal, d_w, and amplitude, d_a, domains. Two additional markers, d_w^{NL} and d_a^{NL}, restricted to measure the nonlinear information present within d_w and d_a are also proposed.** ***Methods:*** **We evaluated the accuracy of the proposed markers in capturing T-wave time and amplitude variations in 3 situations: 1) In a simulated set up with presence of additive Laplacian noise, 2) when modifying the spatio-temporal distribution of electrical repolarization with an electro-physiological cardiac model, and 3) in ECG records from healthy subjects undergoing a tilt table test.** ***Results:*** **The metrics d_w, d_a, d_w^{NL}, and d_a^{NL} followed T-wave time- and amplitude-induced variations under different levels of noise, were strongly associated with changes in the spatio-temporal dispersion of repolarization, and showed to provide additional information to differences in the heart rate, QT and T_{pe} intervals, and in the T-wave width and amplitude.** ***Conclusion:*** **The proposed ECG-derived markers robustly quantify T-wave morphological variability, being strongly associated with changes in the dispersion of repolarization.** ***Significance:*** **The proposed ECG-derived markers can help to quantify the variability in the dispersion of ventricular repolarization, showing a great potential to be used as arrhythmic risk predictors in clinical situations.**

***Index Terms*—Electrocardiogram, morphological variability, repolarization, T-wave, time-warping.**

I. Introduction

VENTRICULAR arrhythmias are an important cause of morbidity and sudden cardiac death (SCD) in almost all forms of heart disease. Detection and prevention of arrhythmic events are the main strategies to decrease SCD outcomes [1]. Enhanced spatio-temporal repolarization heterogeneity is related to the generation of ventricular arrhythmias that could lead to SCD [2], and increased spatio-temporal repolarization variability has been linked to increased arrhythmic risk [3] in both beat-to-beat (short-term) scenarios [4], [5], and when measuring at different stable heart rates [6], [7]. The T-wave on the electrocardiogram (ECG) reflects the spatio-temporal dispersion of repolarization times of the ventricular myocites, with homogeneous increments of this dispersion being reflected as both linear and nonlinear variations of the T-wave width and amplitude, and enhanced heterogeneities being manifested as additional nonlinear deformations of the T-wave, such as notches or asymmetries [8]–[10].

Previous techniques developed to investigate cardiac repolarization from the surface ECG were based on interval repolarization durations and have been shown to reflect spatio-temporal repolarization heterogeneity [11], [12], such as the QT interval, its corrected version [13], T-wave width [14], the distance from the peak to the end of the T wave (T_{pe} interval) [15], the dynamic changes in the T_{pe} interval with respect to the heart rhythm [16], the variability of the QT interval [3], the T-wave alternans [17], or the ST elevation [18]. However, these markers might not be able to capture both linear and nonlinear T-wave morphological variations, and extracting such information may provide improved ventricular arrhythmic risk. Although this limitation has been faced by recent indices, including the total cosine R-to-T descriptor, the morphology dispersion index or the T-wave residuum [19], they still lack sufficient superiority and require the information provided by the vectorcardiogram, which could also become a restriction in the clinical practice.

In addition, variations in the temporal domain or misalignments between T-waves might complicate the comparison and corrupt the measurement of amplitude variability. Linear and nonlinear temporal reparameterization (warping) have been used in the literature to overcome this limitation, align ECG waves [20]–[22] and measure amplitude differences with improved accuracy. However, the warping information has never been used as a marker to assess the variability in the time domain.

The objective of this study is to propose and assess the ability of two ECG-derived markers, d_w, and d_a, and their nonlinearly restricted versions, d_w^{NL} and d_a^{NL}, to quantify single-lead T-wave morphological variability. The point-wise

Manuscript received July 1, 2016; revised August 31, 2016; accepted September 29, 2016. Date of publication October 4, 2016; date of current version June 15, 2017. This work was supported in part by the Spanish Ministry of Economy and Competitiveness (MINECO), Spain, under Project TIN2013-41998-R, and in part by the Aragón Government, Spain, and the European Social Fund (EU) through Biomedical Signal Interpretation and Computational Simulation (BSICoS) group. *Asterisk indicates corresponding author.*

*J. Ramírez is with the CIBER-BBN, Zaragoza 50018, Spain, and also with the BSICoS group, I3A, IIS Aragón, University of Zaragoza, Zaragoza 50018, Spain (e-mail: Julia.Ramirez@unizar.es).

M. Orini is with the Institute of Cardiovascular Science, University College London, London NW12BX, U.K., and also with the Barts Heart Centre, London EC1A 7BE, U.K.

J. D. Tucker is with the Sandia National Laboratories, Albuquerque, NM 87015 USA.

E. Pueyo and P. Laguna are with the BSICoS group, University of Zaragoza, Zaragoza 50009, Spain, and also with the CIBER-BBN, Zaragoza 50018, Spain.

Digital Object Identifier 10.1109/TBME.2016.2614899

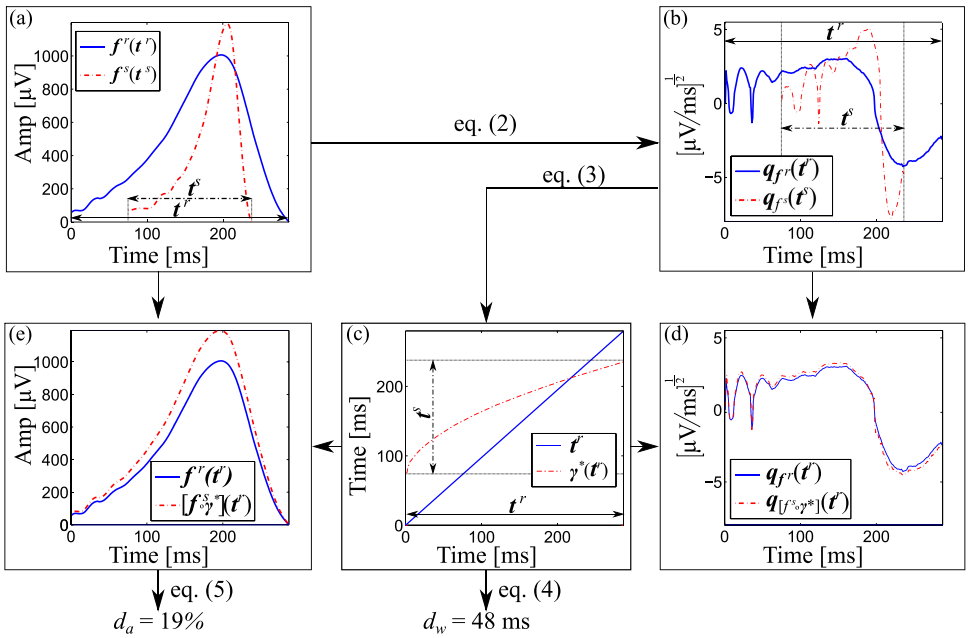

Fig. 1. Diagram flow illustrating the computation of d_w and d_a. (a) Reference T-wave (solid blue) and a T-wave presenting both time and amplitude variability (shorter duration and larger amplitude) (dashed red). (b) Applying (2) we obtain their respective square-root slope functions. (c) Optimizing (3) with the "Dynamic Programming" algorithm (Appendix A), we get $\gamma^*(t^r)$, the warping function that optimally relates t^r and t^s. (e) The reparameterization of $f^s(t^s)$ using $\gamma^*(t^r)$ leads to $[f^s \circ \gamma^*](t^r)$, the warped T-wave with no remaining time domain variability, and only presenting amplitude variability. (d) Square-root slope functions of the reference (solid blue) and warped (dashed red) T-waves.

variability between the temporal domains of different T-waves, or the amount of warping needed to remove the time domain variability, is measured by d_w, while d_a quantifies the point-wise amplitude variability after time warping, or the amplitude variability after removing the temporal domain variability. The markers d_w^{NL} and d_a^{NL} quantify the strictly nonlinear warping and amplitude levels within d_w and d_a, respectively. First, the robustness of d_w, d_a, d_w^{NL}, and d_a^{NL} against noise in a simulated set up is evaluated. Next, an electro-physiological cardiac model is used to investigate the relation between d_w, d_a, d_w^{NL}, and d_a^{NL} and the morphological changes of the action potential at cellular level. Finally, the T-wave morphological variations produced by a tilt test in real ECG are quantified using d_w, d_a, d_w^{NL}, and d_a^{NL}, and their correlation with the heart rate, the QT and T_{pe} intervals, and the T-wave width (TW) and amplitude (TA) is also studied.

II. Methods

A. Mathematical Framework

The methodology used in this work has been adapted from the mathematical framework presented by Srivastava *et al.* [23]. To exemplify the process of T-wave morphology comparison, consider two T-waves, $f^r(t^r) = [f^r(t^r(1)), \ldots, f^r(t^r(N_r))]^\top$ and $f^s(t^s) = [f^s(t^s(1)), \ldots, f^s(t^s(N_s))]^\top$, where $t^r = [t^r(1), \ldots, t^r(N_r)]^\top$ and $t^s = [t^s(1), \ldots, t^s(N_s)]^\top$ and N_r and N_s being the total duration of t^r and t^s, respectively, as illustrated in Fig. 1(a). We take $f^r(t^r)$ as the reference T-wave and $f^s(t^s)$ as the T-wave to be compared with respect to $f^r(t^r)$.

Let $\gamma(t^r)$ be the warping function that relates t^r and t^s, such that the composition $[f^s \circ \gamma](t^r) = f^s(\gamma(t^r))$ denotes the reparameterization or time domain warping of $f^s(t^s)$ using $\gamma(t^r)$, i.e., $f^s(\gamma(t^r))$ represents the amplitude values of $f^s(t^s)$ if its temporal vector was t^r. A traditional way to find the optimal warping function is

$$\gamma^*(t^r) = \underset{\gamma(t^r)}{\arg\min} \left\{ \| f^r(t^r) - f^s(\gamma(t^r)) \| \right\}. \tag{1}$$

However, this metric has some limitations. Since it is not symmetric, $(\| f^r(t^r) - f^s(\gamma(t^r)) \| \neq \| f^s(t^s) - f^r(\gamma^{-1}(t^s)) \|)$, it is not a proper distance and can lead to degenerate results if $f^r(t^r)$ and $f^s(t^s)$ present variations in the amplitude domain ("pinching effect") [24]. To address this, the square-root slope function (SRSF) was proposed [23], [25] to solve the warping in a well-defined geometrical space by warping, instead, the SRSFs, defined as the square-root of the derivative of $f(t)$, considering the sign

$$q_f(t) = \mathrm{sign}\left(\dot{f}(t)\right)\sqrt{\left|\dot{f}(t)\right|}. \tag{2}$$

The SRSF of $f^r(t^r)$ and $f^s(t^s)$, $q_{f^r}(t^r)$ and $q_{f^s}(t^s)$, respectively, are shown in Fig. 1(b). Now, the optimal warping function is the one that minimizes the amplitude difference between the SRSF of $f^r(t^r)$ and $f^s(\gamma(t^r))$, $q_{f^r}(t^r)$ and $q_{[f^s \circ \gamma]}(t^r) = q_{f^s}(\gamma(t^r))\sqrt{\dot{\gamma}(t^r)}$, respectively [23], [25]

$$\begin{aligned}\gamma^*(t^r) &= \underset{\gamma(t^r)}{\arg\min} \left(\left\| q_{f^r}(t^r) - q_{[f^s \circ \gamma]}(t^r) \right\| \right) \\ &= \underset{\gamma(t^r)}{\arg\min} \left(\left\| q_{f^r}(t^r) - q_{f^s}(\gamma(t^r))\sqrt{\dot{\gamma}(t^r)} \right\| \right).\end{aligned} \tag{3}$$

The dynamic programming algorithm, explained in Appendix A, was used to obtain the solution of this optimization [26]. The metric minimized in (3) is a proper distance, which overcomes the limitation of the metric minimized in (1) [23],

[25], [27]. The optimal warping function, $\boldsymbol{\gamma}^*(\boldsymbol{t}^r)$, that optimally warps $\boldsymbol{f}^r(\boldsymbol{t}^r)$ and $\boldsymbol{f}^s(\boldsymbol{t}^s)$ is shown in Fig. 1(c). The warped T-wave, $\boldsymbol{f}^s(\boldsymbol{\gamma}^*(\boldsymbol{t}^r))$ is shown in Fig. 1(e), together with the reference T-wave, $\boldsymbol{f}^r(\boldsymbol{t}^r)$, while their corresponding SRSFs are shown in Fig. 1(d).

The level of warping may be different under various situations and it reflects important information regarding time domain variability. We define a metric, d_w, that quantifies the level of warping needed to optimally align any two T-waves as the average of the absolute difference value between $\boldsymbol{\gamma}^*(\boldsymbol{t}^r)$ and $\boldsymbol{t}^r$

$$d_w = \frac{1}{N_r}\sum_{n=1}^{N_r} \left|\gamma^*\left(t^r\left(n\right)\right) - t^r\left(n\right)\right|. \tag{4}$$

If $\boldsymbol{\gamma}^*(\boldsymbol{t}^r) = \boldsymbol{t}^r$, then the functions are perfectly aligned. Therefore, it makes sense to use the difference between $\boldsymbol{\gamma}^*(\boldsymbol{t}^r)$ and $\boldsymbol{t}^r$ to quantify the variability between each T-wave time domain. Fig. 1 shows the value of d_w quantifying the time variability between $\boldsymbol{f}^r(\boldsymbol{t}^r)$ and $\boldsymbol{f}^s(\boldsymbol{t}^s)$. Once the time domain variability has been compensated for by optimally warping $\boldsymbol{f}^s(\boldsymbol{t}^s)$, the remaining variability is merely amplitude variability, as shown in Fig. 1(e). Therefore, the amplitude difference between $\boldsymbol{f}^r(\boldsymbol{t}^r)$ and $\boldsymbol{f}^s(\boldsymbol{\gamma}^*(\boldsymbol{t}^r))$, i.e., the variability between $\boldsymbol{f}^r(\boldsymbol{t}^r)$ and $\boldsymbol{f}^s(\boldsymbol{t}^s)$ not due to deviations in the time domain, is quantified as the area contained between $\boldsymbol{f}^r(\boldsymbol{t}^r)$ and $\boldsymbol{f}^s(\boldsymbol{\gamma}^*(\boldsymbol{t}^r))$, normalized by the L2-norm of $\boldsymbol{f}^r(\boldsymbol{t}^r)$

$$d_a = \frac{e_a}{\|e_a\|}\cdot\frac{\|\boldsymbol{f}^s\left(\boldsymbol{\gamma}^*\left(\boldsymbol{t}^r\right)\right) - \boldsymbol{f}^r\left(\boldsymbol{t}^r\right)\|}{\|\boldsymbol{f}^r\left(\boldsymbol{t}^r\right)\|}\times 100 \tag{5}$$

where $\frac{e_a}{\|e_a\|}, e_a = \sum_{n=1}^{N_r}(f^s\left(\gamma^*\left(t^r\right)\right) - f^r\left(t^r\right))$ accounts for the sign. Fig. 1 shows the value of d_a, measuring the amplitude variability between $\boldsymbol{f}^r(\boldsymbol{t}^r)$ and $\boldsymbol{f}^s(\boldsymbol{t}^s)$.

B. Extracting Nonlinear T-Wave Morphological Variability

The proposed markers, d_w and d_a, contain information about linear and nonlinear differences in both time and amplitude, respectively. Isolating the strictly nonlinear variability information might provide additional understanding on the different sources generating the morphology of the T-wave.

Fig. 2(a), shows the optimal warping function from Fig. 1(c). As explained in (4), the marker d_w is calculated as the mean deviation of $\boldsymbol{\gamma}^*(\boldsymbol{t}^r)$ from $\boldsymbol{t}^r$, marked in yellow in Fig. 2(a). By fitting $\boldsymbol{\gamma}^*(\boldsymbol{t}^r)$ with a linear regression, $\boldsymbol{\gamma}_l^*(\boldsymbol{t}^r)$, (black dashed line), and measuring the mean deviation of $\boldsymbol{\gamma}^*(\boldsymbol{t}^r)$ with respect to this regression, we can have a quantification of the level of nonlinear warping (dashed cyan region). This can be expressed as

$$d_w^{\mathrm{NL}} = \frac{1}{N_r}\sum_{n=1}^{N_r}\left|\gamma^*\left(t^r\left(n\right)\right) - \gamma_l^*\left(t^r\left(n\right)\right)\right| \tag{6}$$

where $\boldsymbol{\gamma}_l^*(\boldsymbol{t}^r)$ is the linear fitting of $\boldsymbol{\gamma}^*(\boldsymbol{t}^r)$ using the least absolute residual method [28] [see Fig. 2(a)]. The linear warping can be quantified by measuring the mean deviation of $\boldsymbol{\gamma}_l^*(\boldsymbol{t}^r)$ from $\boldsymbol{t}^r$ [nondashed region in Fig. 2(a)].

Regarding d_a, normalizing the warped T-waves, we can quantify nonlinear amplitude differences not due to homogeneous scaling, and possibly caused by heterogeneous dispersion of repolarization times

$$d_a^{\mathrm{NL}} = \left\|\frac{\boldsymbol{f}^r\left(\boldsymbol{t}^r\right)}{\|\boldsymbol{f}^r\left(\boldsymbol{t}^r\right)\|} - \frac{\boldsymbol{f}^s\left(\boldsymbol{\gamma}^*\left(\boldsymbol{t}^r\right)\right)}{\|\boldsymbol{f}^s\left(\boldsymbol{\gamma}^*\left(\boldsymbol{t}^r\right)\right)\|}\right\|\times 100. \tag{7}$$

This is depicted in Fig. 2(b). Fig. 2(b.1) shows the reference, $\boldsymbol{f}^r(\boldsymbol{t}^r)$ (solid blue), and studied, $\boldsymbol{f}^s(\boldsymbol{t}^s)$ (dashed red), T-waves with only amplitude variability (we assumed $\boldsymbol{\gamma}^*(\boldsymbol{t}^r) = \boldsymbol{t}^r$ in this example for clarity). Fig. 2(b.2) shows the remaining nonlinear amplitude variability after normalization.

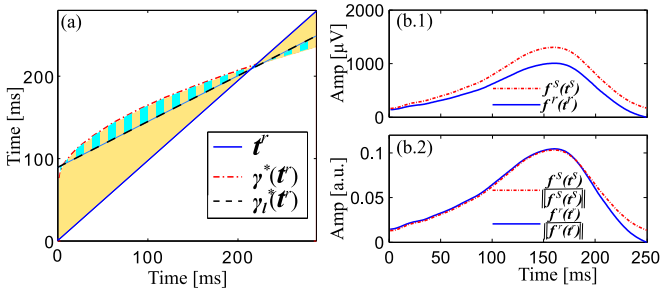

Fig. 2. Calculation of the nonlinear warping and amplitude information. (a) The area between $\boldsymbol{\gamma}^*(\boldsymbol{t}^r)$ and $\boldsymbol{t}^r$ (yellow region) represents the total warping information, quantified by d_w, while the area between $\boldsymbol{\gamma}^*(\boldsymbol{t}^r)$ and $\boldsymbol{\gamma}_l^*(\boldsymbol{t}^r)$ represents the nonlinear warping information (dashed cyan region), quantified by d_w^{NL}. (b.1) Reference, $\boldsymbol{f}^r(\boldsymbol{t}^r)$ (solid blue), and studied, $\boldsymbol{f}^s(\boldsymbol{t}^s)$ (dashed red), T-waves with only amplitude variability ($\boldsymbol{\gamma}^*(\boldsymbol{t}^r) = \boldsymbol{t}^r$). (b.2) Normalized reference, $\frac{\boldsymbol{f}^r(\boldsymbol{t}^r)}{\|\boldsymbol{f}^r(\boldsymbol{t}^r)\|}$, and studied, $\frac{\boldsymbol{f}^s(\boldsymbol{\gamma}^*(\boldsymbol{t}^r))}{\|\boldsymbol{f}^s(\boldsymbol{\gamma}^*(\boldsymbol{t}^r))\|}$, T-waves.

C. Signal Preprocessing and T-Wave Extraction

Preprocessing of the ECG signals included low-pass filtering at 40 Hz with a butterworth filter of order 6 to remove electric and muscle noise but still allow QRS detection, cubic splines interpolation for baseline wander removal, and ectopic beats detection.

A single-lead-plus-rules delineation technique [29] was applied over all leads in the ECG record to delimitate the T-waves. Then, principal component analysis was calculated lead-wise over the selected T-waves to emphasize the T-wave components, improve its delineation, and enhance morphological differences [30]. Finally, the first principal component was further delineated using a single-lead technique [31], and the T-waves were confined from the T-wave onset and T-wave end delineation marks. Then, each T-wave was further low-pass filtered at 20 Hz using a butterworth filter of order 6 to remove remaining out-of-band high frequency components that could potentially corrupt the T-wave shape. The filtered T-waves were visually checked for artifacts related to onset/end filtering discontinuities, observing no issues in this respect.

Before applying the warping algorithm, the reference and the studied T-waves were aligned according to their gravity centers, so that $\boldsymbol{\gamma}^*(\boldsymbol{t}^r)$ is only dependent on changes in the T-wave morphology, and not on global shifts. The center of gravity was calculated as the shift in $\boldsymbol{t}^s$ that offered the maximum cross-correlation between $\boldsymbol{f}^r$ and $\boldsymbol{f}^s$. In case $\boldsymbol{f}^r$ and $\boldsymbol{f}^s$ had different polarities, $\boldsymbol{f}^s$ was inverted to match the polarity of $\boldsymbol{f}^r$.

III. Data Sets

A. Simulated Variability in a Computer-Generated ECG

The accuracy of d_w, d_a, d_w^{NL}, and d_a^{NL} in capturing linear and nonlinear T-wave time and amplitude variations was assessed by simulating controlled variations in the T-wave duration and amplitude under the presence of different levels of additive noise.

Let the T-wave from a reference noise-free cardiac beat, sampled at 1 kHz, be the reference T-wave, $\boldsymbol{f}^r(\boldsymbol{t}^r)$. This reference cardiac beat was obtained from the first principal component, calculated as described in Section II-C, over the eight-standard leads recorded at supine position from a healthy subject.

The nonlinear T-wave amplitude variability was modeled by adding a sinusoidal wave, of period 0.25 times N_r and amplitude function of each beat, to $\boldsymbol{f}^r(\boldsymbol{t}^r)$ in the following way:

$$\begin{aligned}\boldsymbol{f}_i^{\mathrm{NL}}(\boldsymbol{t}^r) &= \boldsymbol{f}^r(\boldsymbol{t}^r) + c(i)\cdot\sin\left(2\pi\frac{1}{4N_r}\boldsymbol{t}^r\right),\\ c(i) &= 150.\sin\left(\frac{\pi\left(\frac{I}{2}+i-1\right)}{I}\right), \quad i=1,\ldots,I \end{aligned} \tag{8}$$

where i is the heart beat index. Then, the T-wave linear amplitude variability was modeled by multiplying the deviations from the iso-electric line of $\boldsymbol{f}_i^{\mathrm{NL}}(\boldsymbol{t}^r)$ by a factor sinusoidally modulated across beats

$$\boldsymbol{f}_i^s(\boldsymbol{t}^r) = \boldsymbol{f}_i^{\mathrm{NL}}(\boldsymbol{t}^r)\cdot\left(1+0.15\cdot\sin\left(\frac{\pi\left(\frac{I}{2}+i-1\right)}{I}\right)\right). \tag{9}$$

Next, linear variations in the duration of the T-wave were simulated according to

$$\boldsymbol{t}_i^l = \boldsymbol{\gamma}_i(\boldsymbol{t}^r), \quad i=1,\ldots,I \tag{10}$$

where now $\boldsymbol{\gamma}_i(\boldsymbol{t}^r)$ is the operator that up- and downsamples $\boldsymbol{t}^r$ according to the sampling factor, $\alpha(i)$

$$\alpha(i) = \frac{0.6\cdot(i-1)}{(I-1)} + 0.7, \quad i=1,\ldots,I \tag{11}$$

when simulating large time variations [like those found under appreciably different RR values, which for a reference $RR=1$ s, would produce an RR spanning from $RR=0.7$ s (85 beats per minute (bpm)) to $RR=1.3$ s (46 bpm), representing a heart rhythm change after moving from activity to relax, as an example, [32]] and

$$\alpha(i) = \frac{0.2\cdot(i-1)}{(I-1)} + 0.9, \quad i=1,\ldots,I \tag{12}$$

when simulating small time variations [like those found when analyzing short-term variability, which for a reference $RR=1$ s, would produce an RR spanning from $RR=0.9$ s (66 bpm) to $RR=1.1$ s (54 bpm), representing the beat-to-beat heart rate variability under stationary conditions [32]].

Nonlinear variations in the temporal domain of the T-wave were introduced by adding a sinusoidal modulation of period N_r and linearly varying amplitude, guaranteeing a monotonic increasing function

$$\begin{aligned}\boldsymbol{t}_i^s &= \boldsymbol{t}_i^l + d(i)\frac{N_r}{N_{s_i}}\cdot\sin\left(2\pi\frac{1}{N_r}\boldsymbol{t}_i^l\right),\\ d(i) &= \frac{30(i-1)}{I-1} - 15, \quad i=1,\ldots,I\end{aligned} \tag{13}$$

where N_{s_i} is, now, the duration of $\boldsymbol{t}_i^l$.

The reparameterized ith T-wave was, then, obtained using

$$\boldsymbol{f}_i^s(\boldsymbol{t}_i^s) = \boldsymbol{f}_i^s\left(\boldsymbol{\gamma}_i(\boldsymbol{t}^r) + d(i)\frac{N_r}{N_{s_i}}\cdot\sin\left(2\pi\frac{1}{N_r}\boldsymbol{\gamma}_i(\boldsymbol{t}^r)\right)\right). \tag{14}$$

The ith modulated cardiac beat was obtained by transforming $\boldsymbol{f}^r(\boldsymbol{t}^r)$ to $\boldsymbol{f}_i^s(\boldsymbol{t}_i^s)$. A simulated ECG signal was obtained by concatenating the $I=300$ modulated cardiac beats. This led to a 300-beat ECG signal, which was filtered as explained in Section II-C, and the T-waves were selected using the known delimitation marks. The morphological average of the 300 T-waves, $\bar{\boldsymbol{f}}(\boldsymbol{t}^r)$, was obtained with the algorithm explained in Appendix B, and this mean warped T-wave was chosen as the reference for comparison.

The reference $\boldsymbol{d}_w^r = [d_w^r(1),\ldots,d_w^r(I)]$, $\boldsymbol{d}_a^r = [d_a^r(1),\ldots,d_a^r(I)]$, $\boldsymbol{d}_w^{\mathrm{NL}^r} = [d_w^{\mathrm{NL}^r}(1),\ldots,d_w^{\mathrm{NL}^r}(I)]$, and $\boldsymbol{d}_a^{\mathrm{NL}^r} = [d_a^{\mathrm{NL}^r}(1),\ldots,d_a^{\mathrm{NL}^r}(I)]$ series were obtained by comparing each $\boldsymbol{f}_i^s(\boldsymbol{t}_i^s)$ with $\bar{\boldsymbol{f}}(\boldsymbol{t}^r)$, following the procedure explained in Section II-A.

Then, zero mean Laplacian noise was iteratively added to the simulated ECG signal, such that the signal-to-noise ratio (SNR) was, in decibels (dB): $\mathrm{SNR}=\{5,10,\ldots,35\}$. The estimated $\boldsymbol{d}_w^{\mathrm{SNR}} = [d_w^{\mathrm{SNR}}(1),\ldots,d_w^{\mathrm{SNR}}(I)]$, $\boldsymbol{d}_a^{\mathrm{SNR}} = [d_a^{\mathrm{SNR}}(1),\ldots,d_a^{\mathrm{SNR}}(I)]$, $\boldsymbol{d}_w^{\mathrm{NL}^{\mathrm{SNR}}} = [d_w^{\mathrm{NL}^{\mathrm{SNR}}}(1),\ldots,d_w^{\mathrm{NL}^{\mathrm{SNR}}}(I)]$, and $\boldsymbol{d}_a^{\mathrm{NL}^{\mathrm{SNR}}} = [d_a^{\mathrm{NL}^{\mathrm{SNR}}}(1),\ldots,d_a^{\mathrm{NL}^{\mathrm{SNR}}}(I)]$ series were obtained by comparing the T-waves from the noisy modulated ECG signal, after preprocessing as explained in Section II-C, with their mean warped T-wave. The normalized relative errors were, then, calculated as

$$e_d(\mathrm{SNR}) = \sqrt{\frac{\sum_{i=1}^{I}\left(d^{\mathrm{SNR}}(i)-d^r(i)\right)^2}{\sum_{i=1}^{I}\left(d^r(i)\right)^2}}\times 100 \tag{15}$$

where $d=\{d_w,d_a,d_w^{\mathrm{NL}},d_a^{\mathrm{NL}}\}$. The noise generation and relative error measurement steps were repeated 50 times to have robust relative error values.

B. Simulated Variability in an Electro-Physiological Model

The relation between changes in myocardial repolarization dynamics and d_w, d_a, d_w^{NL}, and d_a^{NL} was explored using an electro-physiological model [33], as described in Appendix C. This model presents a formalization of the forward problem in which action potentials at M ventricular sites are projected onto the body surface. The action potentials repolarization time at each cardiac site m is given by $\rho_m = \bar{\rho} + \Delta\rho_m$, where $\bar{\rho}$ is the mean repolarization time and $\Delta\rho_m$ represents the deviation of the local repolarization time at cardiac site m from $\bar{\rho}$. The standard deviation of $\Delta\rho_m$, σ, is a measure of the global dispersion of repolarization. Ventricular action potential data was obtained

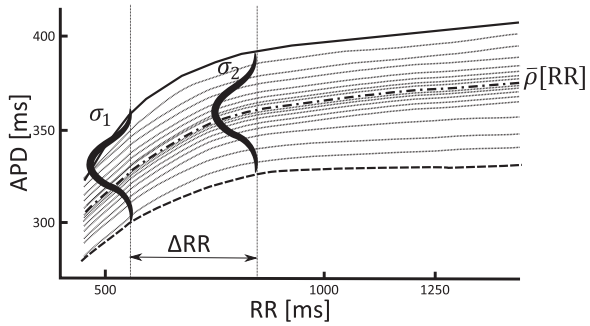

Fig. 3. Dynamic restitution curves between different ventricular regions. σ indicates the standard deviation of the repolarization times dispersion at each value of RR interval.

from a normal male, and the ECG leads were calculated as described in Appendix C. Next, principal component analysis was performed over the ECG leads and the first principal component was preprocessed and delineated as explained in Section II-C. The extracted T-wave was considered as the reference T-wave in this simulation study.

We assessed the morphological variability reflected on the jth T-wave using d_w, d_a, d_w^{NL}, and d_a^{NL}, where $j = 1, \ldots, 5$ is the level of variation in ρ_m at each situation, under four scenarios

1) Lengthening of the mean repolarization time, $\bar{\rho}$, according to the following equation:

$$\bar{\rho}\,(j) = \bar{\rho} + 25 \cdot (j-1)\,, \quad j = 1, \ldots, 5 \tag{16}$$

where $\bar{\rho}(j)$ is in ms. This is equivalent to move from a beat with σ_1 to other beat with $\sigma_2 = \sigma_1$ and different $\bar{\rho}$, if $\bar{\rho}$ is varying with the RR interval (see Fig. 3).

2) Increasing the repolarization time dispersion, σ, using the following equation:

$$\begin{aligned} \Delta\rho_m\,(j) &= \Delta\rho_m\,(1 + 0.2\,(j-1))\,, \quad j = 1, \ldots, 5 \\ \sigma\,(j) &= \sqrt{\frac{1}{M-1}\sum_{m=1}^{M}\left(\Delta\rho_m\,(j) - \bar{\rho}\right)^2} \end{aligned} \tag{17}$$

where $\Delta\rho_m\,(j)$ and $\sigma(j)$ are in ms. This is equivalent to move from a beat with σ_1 to a beat with $\sigma_2 \neq \sigma_1$ and same $\bar{\rho}$ (see Fig. 3).

3) In the third scenario we combined simulations 1 and 2.

4) Progressive variations of the epicardial action potential durations (APDs), defined as the difference between the maximum repolarization and depolarization slopes, (by only modifying the repolarization times, ρ_m, of epicardial nodes) toward the mean endocardial APD. This emulates the reduction in the dispersion of repolarization after reducing the spatial heterogeneity of I_{ks} current as reported in [10].

Principal component analysis was performed on the resulting ECG leads, and the first principal component was preprocessed and delineated as explained in Section II-C. The subsequent $d_w(j)$, $d_a(j)$, $d_w^{\mathrm{NL}}(j)$, and $d_a^{\mathrm{NL}}(j)$ series were obtained for each scenario by comparing the resulting jth T-wave with the reference T-wave.

C. Real ECG

In this section, we focused the ECG study on the tilt table test since it is a standard procedure that induces variations in the modulation of the autonomic nervous system, i.e., heart rate, and in the repolarization features, i.e., T-wave morphology [16]. Therefore, our objective was to evaluate the ability of d_w, d_a, d_w^{NL}, and d_a^{NL} to capture the T-wave morphological changes induced by the orthostatic stress, and their interaction with changes in the heart rate. ECG recordings from 17 healthy subjects (age 28.5 $\pm$ 2.8 years, 11 males) with no previous medical history related to cardiovascular diseases, acquired at the University of Zaragoza (ANS-UZ database) were analyzed [16]. Each recording consisted of eight ECG leads, sampled at 1 KHz, acquired during a 13-min head-up tilt test (4-min supine, 5 min at 70°, 4-min supine). Each eight-lead ECG signal was preprocessed and the T-waves from every beat were delimited as explained in Section II-C.

We assumed stationariness in three windows, $early\ supine$ (ES), $Tilt$ (TL), and $late\ supine$ (LS), as done in [34]. These windows had a length of 20 beats and finished 30 s before any transition during the tilt test. Then, for each subject and window, we calculated the RR, QT, TW, and T_{pe} interval values as the differences between subsequent QRS fiducial points, T-wave end and QRS complex onset, T-wave end and T-wave onset, and T-wave end and T-wave peak, respectively, from the annotation marks calculated in Section II-C [31]. Similarly, the TA values were obtained from the T-wave amplitude values. Finally, for each subject and window, we calculated the median RR, QT, TW, T_{pe}, and TA values. In addition, the mean warped T-wave of the 20 T-waves in each window and subject was calculated following the algorithm explained in Appendix B.

1) Analysis of Long-Term T-Wave Morphological Variability: To evaluate the variations of the T-wave produced by the orthostatic stress, we compared each mean warped T-wave with the other two [(LS - ES), (TL - ES), and (LS - TL)], and we calculated the difference between each median RR, T_{pe}, TW, QT, and TA values and the other two, obtaining three values of d_w, d_a, d_w^{NL}, d_a^{NL}, ΔRR, ΔT_{pe}, ΔTW, ΔQT, and ΔTA per subject.

2) Analysis of Short-Term T-Wave Morphological Variability: To evaluate the variability of the T-wave at steady-state conditions, we calculated the median absolute deviation of QT, TW, T_{pe}, and TA with respect to their median value, for each subject and window [35]. Regarding the proposed morphological markers, we calculated the median of the 20 absolute values of d_w, d_a, d_w^{NL}, and d_a^{NL}, obtained when comparing each T-wave in the window with its mean warped T-wave. Finally, we measured the SNR value of the T-waves in the window, defined as the ratio between the root mean squared values of their arithmetic mean T-wave and the difference between each T-wave and this arithmetic mean T-wave, in decibels. Therefore, we assumed that noise level was higher than the variability itself. This definition can be argued at situations where the T-wave variability is high, as compared to noise. However, for Holter ECG records at stationary conditions, it is expected to have low T-wave variability and high noise levels. Then, for general

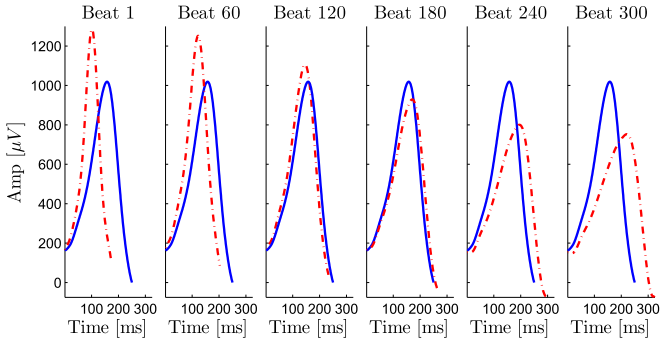

Fig. 4. Evolution of linear and nonlinear time and amplitude simulated variations. The reference T-wave, $\boldsymbol{f}^r(\boldsymbol{t}^r)$, is displayed in solid blue, and the simulated T-wave, $\boldsymbol{f}_i^s(\boldsymbol{t}_i^s)$, is plotted in dashed red, for $i = \{1, 60, 120, 180, 240, 300\}$.

cases, this will be an appropriate assumption when estimating correlation for the whole range of SNR.

3) Statistical Analysis: The Spearman's correlation coefficient was used to quantify the strength of the linear correlation. The Wilcoxon signed rank test was used in pairwise comparisons. A p value of ≤ 0.05 was considered as statistically significant. On each boxplot, the central mark is the median, the edges of the box are the 25th and 75th percentiles, and the whiskers extend to the most extreme data points not considered as outliers. The notches represent the 95% confidence interval of the median, calculated as $q2 \pm 1.57(q3-q1)/\sqrt{n}$, where $q2$ is the median, $q1$ and $q3$ are the 25th and 75th percentiles, respectively, and n is the number of subjects. Therefore, since the sample is small (17 subjects), the notches might extent beyond the end of the box in some cases. Computations were executed using MATLAB 7.10.0 (2010a), Intel Core i7-2600 CPU, 3.40 GHz, 8.00 GB RAM.

IV. Results

A. Simulated Variability in a Computer-Generated ECG

Fig. 4 shows six examples of the linear and nonlinear time and amplitude simulations of the T-wave. The reference T-wave, $\boldsymbol{f}^r(\boldsymbol{t}^r)$ is displayed in solid blue in every panel, and the simulated T-wave, $\boldsymbol{f}_i^s(\boldsymbol{t}_i^s)$ is plotted in dashed red, for $i = \{1, 60, 120, 180, 240, 300\}$.

Fig. 5 shows the evolution of d_w^r (a), d_a^r (b), $d_w^{\mathrm{NL}^r}$ (c), and $d_a^{\mathrm{NL}^r}$ (d) series as the linear and nonlinear time and amplitude modulations induced in the T-wave change. The evolution of d_w^{20}, d_a^{20}, $d_w^{\mathrm{NL}^{20}}$, and $d_a^{\mathrm{NL}^{20}}$ is illustrated in red.

Fig. 6 shows the relative error between $\boldsymbol{d}_w^{\mathrm{SNR}}$ and $\boldsymbol{d}_w^r$ (a), $\boldsymbol{d}_a^{\mathrm{SNR}}$ and $\boldsymbol{d}_a^r$ (b), $\boldsymbol{d}_w^{\mathrm{NL}^{\mathrm{SNR}}}$ and $\boldsymbol{d}_w^r$ (c), and $\boldsymbol{d}_a^{\mathrm{NL}^{\mathrm{SNR}}}$ and $\boldsymbol{d}_a^r$ (d), for different SNR when simulating large (red) and small (black) linear time variations.

B. Simulated Variability in an Electro-Physiological Model

Fig. 7(a) shows the simulation of the first scenario described in Section III-B, i.e., lengthening of the mean repolarization time, $\bar{\rho}$. Fig. 7(b) illustrates the simulation of the second scenario,

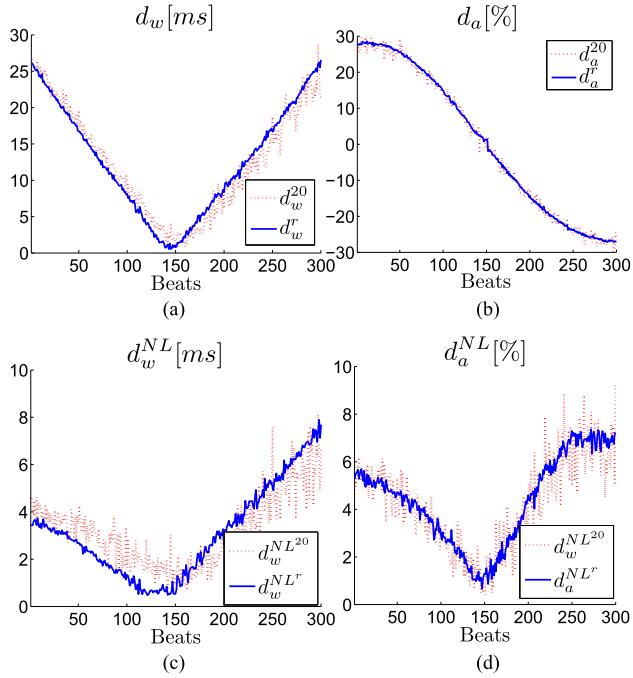

Fig. 5. Evolution of d_w, d_a, d_w^{NL}, and d_a^{NL} with respect to the level of linear and nonlinear time and amplitude modulations in a noise-free scenario (solid blue) and under the presence of additive Laplacian noise with SNR = 20 dB (dashed red), when simulating large temporal variations, as in (11).

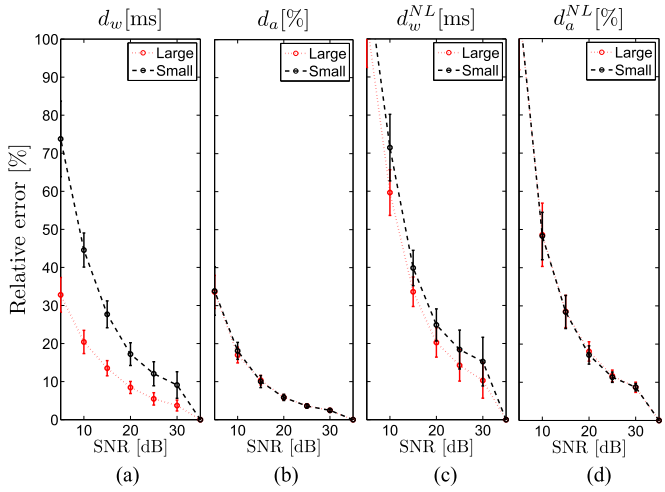

Fig. 6. Relative error between reference and estimated d_w, d_a, d_w^{NL}, and d_a^{NL} under the presence of additive Laplacian noise, when simulating large (solid) and small (dotted) time variations, as in (11) and (12), respectively. Nonlinear time variations and linear and nonlinear amplitude changes are the same in all situations.

i.e., an increment of the dispersion of action potential repolarization times, σ. Fig. 7(c) shows the combined simulation of $\bar{\rho}$ and σ variation. Fig. 7(d) shows the simulation results of the fourth scenario described in Section III-B. Fig. 7(a.1)–(a.3) illustrates the range between the minimum and the maximum APD, with respect to $\bar{\rho}$ (panel a.1), σ (panel b.1), and $\bar{\rho}$ (panel c.1). Fig. 7(d.1) shows an endocardial action potential, which does not change. Fig. 7(a.2), (b.2), and (c.2) illustrates the mean ac-

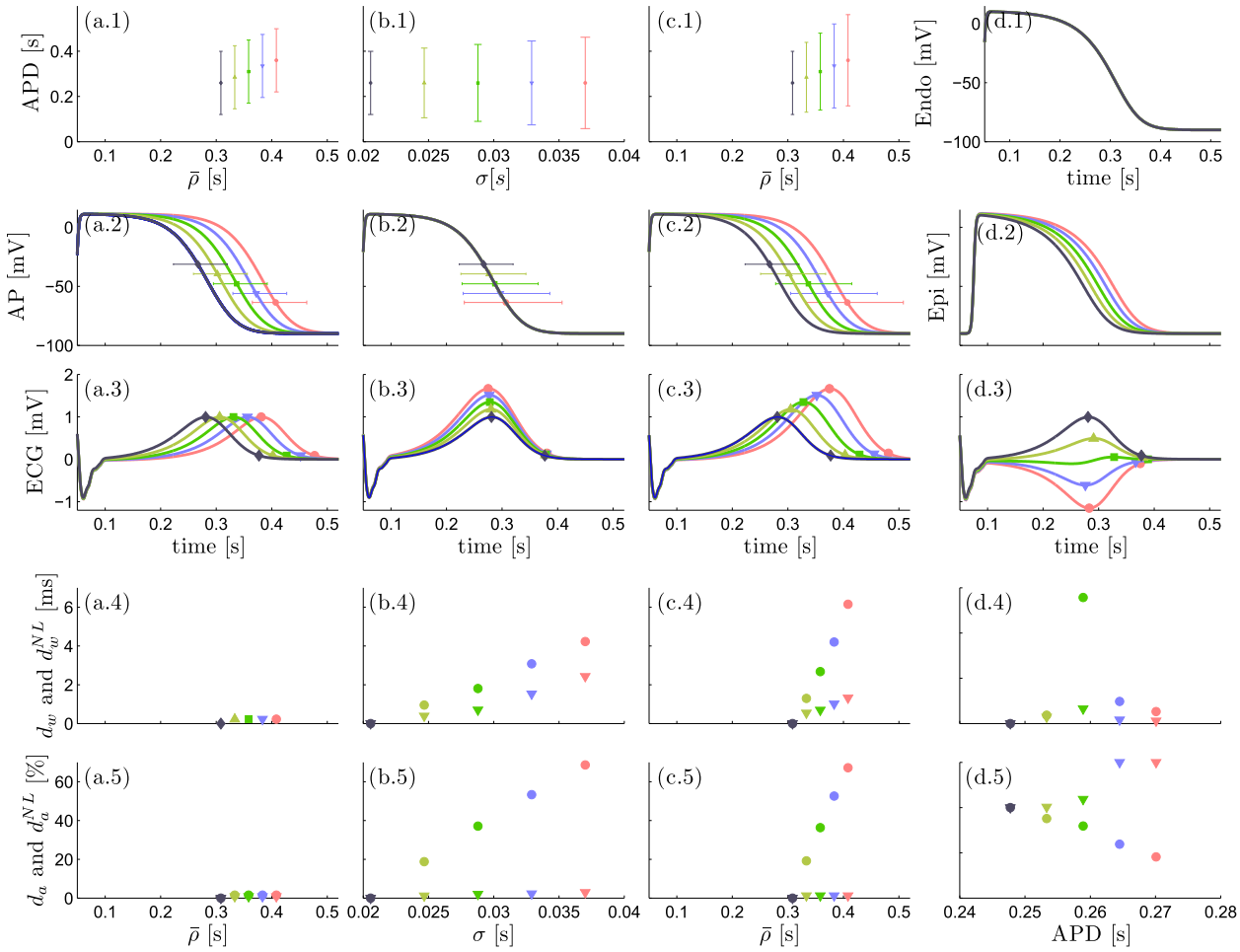

Fig. 7. Performance evaluation using an electro-physiological cardiac model. (a.1)–(a.5), increments of the mean repolarization time, $\bar{\rho}$. (b.1)–(b.5), increments of the standard deviation of the repolarization time dispersion, σ. (c.1)–(c.5), combined variation of $\bar{\rho}$ and σ. (d.1)–(d.5), progressive variations of the epicardial APDs. (a.1)–(c.1): range between the minimum and the maximum APD with respect to the variation. (a.2)–(c.2): mean action potentials with respect to the variation. (d.1)–(d.2): Simulated action potential of endocardial and epicardial cells, respectively. (a.3)–(d.3): ECG beats corresponding to the modified action potentials. (d.4) and (d.5): d_w and d_a values (circles) and d_w^{NL} and d_a^{NL} values (triangles). Each color indicates a level of variation. Horizontal bars represent the range between the minimum and the maximum repolarization time.

tion potential. The horizontal bars represent the corresponding range between the minimum and the maximum repolarization time. It should be noted that they are located slightly away from the mean repolarization time to avoid overlapping with the neighboring horizontal bars, but it is only a matter of display. Fig. 7(d.2) shows an epicardial action potential and the result of progressively increasing its duration (each color represents a different duration). Fig. 7(a.3)–(d.3) shows the principal component as a result of the projection of the modified action potentials. Fig. 7(a.4)–(d.5) shows the values of d_w (circle) and d_w^{NL} (triangle), and of d_a (circle) and d_a^{NL} (triangle), respectively, in the four simulations.

C. Real ECG

1) Analysis of Long-Term T-Wave Morphological Variability: Fig. 8, left column, shows the boxplots of ΔRR (panel a.1), ΔQT, ΔTW, and ΔT_{pe} (panel a.2), ΔTA (panel a.3), d_w, and d_w^{NL} (panel a.4) and d_a and d_a^{NL} (panel a.5) values, measured for (LS-ES), (TL-ES), and (LS-TL).

Table I shows the correlation coefficient, when comparing LS-ES, TL-ES, and LS-TL, between 1) d_w and d_a, and between d_w^{NL} and d_a^{NL}; 2) d_w and d_w^{NL} and each of the repolarization markers measuring time intervals, ΔQT, ΔTW, and ΔT_{pe}; 3) d_a and d_a^{NL} and the repolarization marker measuring amplitude differences, ΔTA; and 4) d_w, d_w^{NL}, d_a, and d_a^{NL} and ΔRR.

2) Analysis of Short-Term T-Wave Morphological Variability: Fig. 8, right column, shows the boxplots of the mean values of RR (panel b.1), median absolute deviation values of QT, TW, and T_{pe} (panel b.2) and TA (panel b.3) with respect to their median value, d_w and d_w^{NL} (panel b.4) and d_a and d_a^{NL} (panel b.5) at the three windows.

Table II shows the correlation coefficient between d_w, d_w^{NL}, d_a, and d_a^{NL}, and the median RR and SNR values for each window separately and when pooling them into a single group $ES+TL+LS$.

D. Computational Time

As a reference for computational time estimation, the calculation of d_w and d_a when comparing two T-waves took 1.31 s

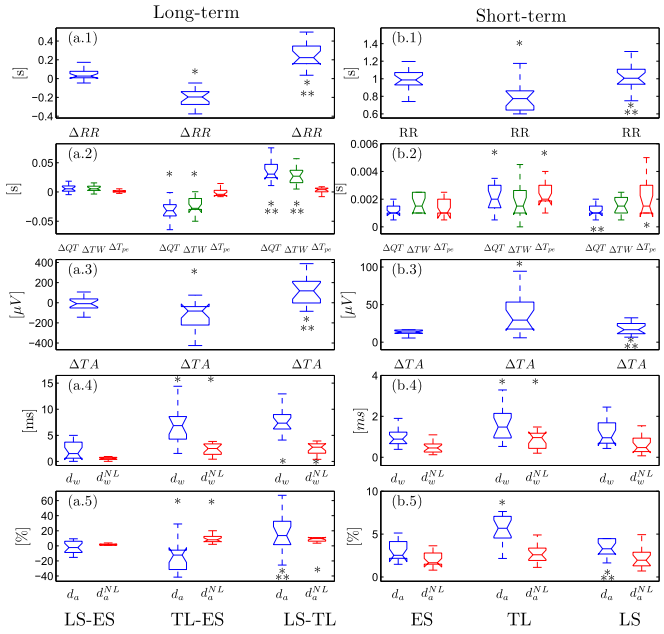

Fig. 8. Left column, boxplots of ΔRR (a.1), ΔQT, $\Delta \mathrm{TW}$, and ΔT_{pe} (a.2), ΔTA (a.3), d_w, and d_w^{NL} (a.4) and d_a and d_a^{NL} (a.5) values, across subjects, between the three windows along the recording. Right column, boxplots of the mean values of RR (b.1), median absolute deviation of QT, TW, and T_{pe} (b.2) and TA (b.3), and mean d_w and d_w^{NL} (b.4) and d_a and d_a^{NL} (b.5) values at the three windows. $*$ indicates statistically significant differences with respect to the leftmost boxplot. $**$ indicates statistically significant differences between the central and rightmost boxplots. It should be noted that left and right panels have different scale.

TABLE I
SPEARMAN'S CORRELATION COEFFICIENT, r, IN THE LONG-TERM ANALYSIS

r	LS-ES	TL-ES	LS-TL
d_w versus d_a	**−0.53**	−0.07	0.23
d_w^{NL} versus d_a^{NL}	**0.72**	**0.77**	**0.69**
d_w versus ΔQT	**0.55**	−0.38	**0.69**
d_w^{NL} versus ΔQT	0.36	−0.36	0.18
d_w versus ΔTW	**0.81**	**−0.60**	**0.71**
d_w^{NL} versus ΔTW	**0.70**	−0.34	0.44
d_w versus ΔT_{pe}	**0.65**	0.10	−0.16
d_w^{NL} versus ΔT_{pe}	0.45	**0.75**	**−0.60**
d_a versus ΔTA	**0.95**	**0.87**	**0.88**
d_a^{NL} versus ΔTA	−0.41	−0.43	0.28
d_w versus ΔRR	**0.55**	−0.41	**0.63**
d_w^{NL} versus ΔRR	0.54	−0.45	0.26
d_a versus ΔRR	−0.07	**0.55**	0.28
d_a^{NL} versus ΔRR	0.36	−0.40	0.44

Significant correlations are indicated in bold.

TABLE II
SPEARMAN'S CORRELATION COEFFICIENT, r, IN THE SHORT-TERM ANALYSIS

r	ES	TL	LS	$ES+TL+LS$
d_w versus SNR	**−0.68**	**−0.60**	**−0.61**	**−0.70**
d_w^{NL} versus SNR	**−0.61**	**−0.55**	**−0.81**	**−0.74**
d_w versus RR	−0.16	**−0.54**	−0.14	**−0.37**
d_w^{NL} versus RR	0.01	−0.40	−0.01	**−0.30**
d_a versus SNR	**−0.93**	**−0.71**	**−0.83**	**−0.85**
d_a^{NL} versus SNR	**−0.90**	**−0.69**	**−0.86**	**−0.84**
d_a versus RR	−0.17	−0.17	−0.09	**−0.39**
d_a^{NL} versus RR	−0.19	−0.41	−0.28	**−0.41**

Significant correlations are indicated in bold.

with the personal computer and software described at the end of Section II. The computation of the mean warped T-wave was slower, needing 47 s to calculate the mean warped T-wave of a set of 20 T-waves. It should be advised that the algorithm has not been optimized in terms of computational time, since the current time is not considered a bottle neck for the technology to be used in clinical practice.

V. DISCUSSION

In this study, we introduced four novel ECG-derived indices, d_w and d_a, that independently quantify T-wave morphological variability in the temporal and amplitude domain, respectively, and d_w^{NL} and d_a^{NL} that isolate the nonlinear information present within d_w and d_a, respectively. We evaluated the accuracy of d_w, d_a, d_w^{NL}, and d_a^{NL} under the presence of additive Laplacian noise. We investigated the relationship between d_w, d_a, d_w^{NL}, and d_a^{NL} and the induced morphological variations at cardiac cellular level and we evaluated the extent of T-wave time and amplitude changes produced by a tilt test in real ECG, and the correlation of d_w, d_a, d_w^{NL}, and d_a^{NL} with the heart rate and with well-known time and amplitude-based repolarization markers.

A. Simulated Variability in a Computer-Generated ECG

The evaluation of the accuracy of d_w, d_a, d_w^{NL}, and d_a^{NL} in detecting linear and nonlinear modulations of the T-wave time domain and amplitude, respectively, in a simulated ECG signal under the presence of additive Laplacian noise confirmed that the four markers were able to robustly and independently capture both modes of variation, with no coupling between the different sources of variability, i.e., the evolution of d_w and d_w^{NL} being independent from that of d_a and d_a^{NL} (see Fig. 5). The values of relative error remained lower than 20% for SNR $=$ 20 dB, indicating that these markers can be robustly used in ambulatory Holter ECG (see Fig. 6). When the simulated time-domain variations were small, the relative error increased for low SNR because noise dominates over time-domain variations of the T-wave.

B. Simulated Variability in an Electro-Physiological Model

The assessment of the relationship between T-wave time and amplitude variations and morphological changes at cardiac cellular level using an electro-physiological cardiac model [33] showed that a variation in the mean repolarization time, $\bar{\rho}$, provoked a shift in the T-wave but with no significant T-wave temporal or amplitude variation [see Fig. 7(a.3)]. Therefore, d_w, d_w^{NL}, d_a, and d_a^{NL} were equal to zero for every $\bar{\rho}(j)$ [see Fig. 7(a.4) and (a.5)]. On the contrary, increments of the dispersion of action potential repolarization times, σ, produced an increment in the range of the APD (panel b.1) and in the range between the minimum and the maximum repolarization time (panel b.2). This led to an homogeneous increment in the amplitude and to a linear and nonlinear increment of the width of the T-wave, which was reflected in higher values of d_w, d_w^{NL}, and d_a, while d_a^{NL} remained zero [panels (b.3)–(b.5)]. The com-

bined variation of $\bar{\rho}$ and σ produced values of d_w, d_w^{NL}, d_a, and d_a^{NL} very similar to those of scenario 2. Progressive increments in the epicardial repolarization time provoked heterogeneous changes in the morphology of the T-wave (panel d.3) and eventually, when the mean epicardial repolarization time was longer than the mean endocardial repolarization time, its inversion. Fig. 7(d.4) and (d.5) illustrate that d_a followed the increment in amplitude variability (due to the T-wave inversion), while d_w measured the asymmetry present in the T-wave when its amplitude was close to zero. In this case, both d_w^{NL} and d_a^{NL} captured the nonlinear time and amplitude, respectively, variations induced by the simulation. These results suggest that d_w, d_w^{NL}, d_a, and d_a^{NL} mainly represent changes in spatio-temporal dispersion of repolarization rather than in its mean, with d_w^{NL} and d_a^{NL} being only sensitive to the variations of spatio-temporal dispersion of repolarization times reflected as nonlinear morphological changes of the T-wave.

C. Real ECG

The purpose of the long-term analysis was to evaluate the ability of the proposed markers to capture the T-wave morphological changes induced by the orthostatic stress, and their interaction with changes in the heart rate. We, then, assumed a similar situation to that from scenario 3, in Section III-B, i.e., variations in repolarization dispersion as a result of variations in heart rate, but in actual ECG records. The orthostatic stress produced significant decrements of the RR, QT, TW, and TA values (see Fig. 8). Regarding T_{pe}, 13 subjects reflected a shorter T_{pe} during TL, while this interval increased for the other 4 subjects. The proposed markers supported these results, showing significant increments in linear and nonlinear temporal and amplitude variations after the orthostatic stress. The correlation analysis (Table I) showed that d_w was correlated with ΔRR, ΔQT, and ΔTW, whereas d_w^{NL} was only correlated with ΔT_{pe}. These results may indicate that the orthostatic stress produces a change in heart rate, inducing linear variations in the QT and TW intervals, which dominate in d_w. The strong correlation between d_w^{NL} and ΔT_{pe} suggests that d_w^{NL} is mainly related to variations in the dispersion of repolarization, independently from changes in heart rate. Regarding the amplitude markers, d_a was highly correlated with ΔTA, whereas d_a^{NL} was completely uncorrelated to it, therefore reflecting information not contained in ΔTA.

The purpose of the short-term analysis was similar to that from scenario 2, in Section III-B, i.e., evaluation of the variations in repolarization dispersion at stable heart rate. Results showed that the variability of QT and T_{pe} intervals, and TA was significantly higher during TL than ES or LS. This was supported by the values of d_w, d_a, and d_w^{NL}, which reflected significantly increased variability in TL as compared to supine (Fig. 8). There was a weak negative correlation between d_w, d_a, d_w^{NL}, and d_a^{NL}, and the median RR (Table II), indicating that the short-term changes in dispersion of repolarization, reflected on the ECG through linear and nonlinear T-wave morphological variations, increase at shorter RR interval values. This may be in corcondance with studies reporting steeper slopes of repolarization restitution at shorter RR values (see Fig. 3) [6]. The correlation values with respect to the SNR indicate that beat-to-beat analysis should be done on clean recordings.

Considering the results of this work and, in view of the large number of publications reporting an association between repolarization instabilities and arrhythmogenesis [3], [13], [17], [18], [36], the proposed methodology might provide additional information that may eventually lead to an improved SCD risk prediction.

D. Technical Considerations

Warping of time domain has often been used in the ECG signal to compensate for the missalignments before measuring amplitude differences, or to quantify time interval variabilities, like those from the QT interval, using linear [37]–[39] and nonlinear [40] time warping. The most common algorithm for nonlinear time warping is the dynamic time warping (DTW) [40], but it fails when the two observed functions also present amplitude variabilities [24]. To prevent this problem, the derivative DTW was proposed [41]. This modification aligns the derivative of the observed functions, rather than their amplitude values. The SRSF used in this work makes the norm to be minimized in (3) to become a proper distance and overcome the "pinching effect," as explained in [23]–[25]. Also, a novel technique to allow for warping in both temporal and amplitude domains has been recently proposed to enable complex adaptations to the morphology of the waveform [22]. The novelty of our work is based on the extraction of indices from the warping information and from the warped signals to quantify the amount of morphological variability.

We applied principal component analysis to obtain a lead projected onto the direction of maximal energy of the T-wave. However, the selection of the lead does not affect the technicalities of the proposed algorithm, since this methodology can be applied to any single lead, which is its main advantage with respect to other methodologies that require the vectorcardiogram, or the information of more than one lead [19].

E. Limitations of the Study

There are several aspects that could influence the estimation reliability of the proposed indices. First, due to the high sensitivity of the warping function, erroneous extraction of the morphology of the T-wave, due to excessive noise or delineation errors, will lead to incorrect values of d_w and d_w^{NL}, and an incorrect warping. Therefore, the markers d_a and d_a^{NL} could also be affected, coupling, in some way, the robustness and sensitivity of the indices. Second, although the proposed markers capture many T-wave morphologies, there can appear extreme morphological variations which will lead to meaningless interpretations of d_w, d_a, d_w^{NL}, and d_a^{NL}. However, we have not found any such extreme variation in the analyzed T-waves, since even for biphasic or S-shaped T-waves we still obtained interpretable results. Next, we selected the first principal component as the lead capturing the direction of maximal variation of the repolarization gradient. Although we assumed that a projection of the maximal energy onto this component also implied a maximal projection of the repolarization variability, given the physiological additive

generation of the ECG signals, this may not always be guaranteed. Finally, this first principal component may be dominated by precordial lead T-waves, which have the highest amplitude and, therefore, in this study, the algorithm did not capture the morphological variation reflected in other leads.

VI. Conclusion

In this study, we introduce two ECG-derived markers, d_w and d_a, and their nonlinearly restricted versions, d_w^{NL} and d_a^{NL}, to quantify single-lead T-wave morphological variability by time-warping metrics. Our findings demonstrate that variations in the dispersion of repolarization, reflected in the ECG through changes in the temporal and amplitude organization of the T-wave, can be robustly captured by d_w and d_a, respectively, with d_w^{NL} and d_a^{NL} measuring the heterogeneous T-wave variations. Future clinical situations will evaluate the strong potential of the proposed markers of T-wave time and amplitude variability to be used as arrhythmic risk predictors.

Appendix A
Dynamic Programming Algorithm

Let $\boldsymbol{f}^r(\boldsymbol{t}^r) = [f^r(t^r(1)), \ldots, f^r(t^r(N_r))]^T$ and $\boldsymbol{f}^s(\boldsymbol{t}^s) = [f^s(t^s(1)), \ldots, f^s(t^s(N_s))]^T$, where $\boldsymbol{t}^r = [t^r(1), \ldots, t^r(N_r)]^T$ and $\boldsymbol{t}^s = [t^s(1), \ldots, t^s(N_s)]^T$ and N_r and N_s being the total duration of $\boldsymbol{t}^r$ and $\boldsymbol{t}^s$, be two given functions and we want to solve for

$$\boldsymbol{\gamma}^*(\boldsymbol{t}^r) = \underset{\boldsymbol{\gamma}(\boldsymbol{t}^r)}{\arg\min} \left(\left\|\boldsymbol{f}^r(\boldsymbol{t}^r) - \boldsymbol{f}^s(\boldsymbol{\gamma}(\boldsymbol{t}^r))\right\|\right) \tag{18}$$

where $\boldsymbol{\gamma}(\boldsymbol{t}^r)$ is a function that matches each point in $\boldsymbol{f}^s(\gamma(\boldsymbol{t}^r))$ with each point in $\boldsymbol{f}^r(\boldsymbol{t}^r)$, and $\boldsymbol{\gamma}^*(\boldsymbol{t}^r)$ is the optimal matching function. We can solve a discrete approximation of this problem using dynamic programming. To decompose the large problem into several subproblems, we define a local cost function

$$E(\tau_1, \tau_2; \boldsymbol{\gamma}) = \left\|\boldsymbol{f}^r(\boldsymbol{\tau}) - \boldsymbol{f}^s(\boldsymbol{\gamma}(\boldsymbol{\tau}))\right\| \quad \tau_1 \le \boldsymbol{\tau} \le \tau_2. \tag{19}$$

So that the original cost function is simply $E(t^r(1), t^r(N_r); \boldsymbol{\gamma})$. A necessary condition for applying dynamic programming to such problems is that the cost function is additive in time. Consider the Two-dimensional time coordinates grid formed by $[\boldsymbol{t}^r, \boldsymbol{t}^s]$, with size $N_r \times N_s$. We will conveniently view γ as a graph in this grid from $[t^r(1), t^s(1)]$ to $[t^r(N_r), t^s(N_s)]$, such that the slope of this graph is always strictly positive. Let $[t^r(a), t^s(b)]$ be a point on the grid. Since we have a constraint on the slope of the graph, there are only certain nodes, N_{ab}, that are allowed to go to $[t^r(a), t^s(b)]$

$$\begin{aligned} N_{\mathrm{ab}} = \; & \{[t^r(a'), t^s(b')] \,|\, t^r(1) \le t^r(a') < t^r(a), \\ & t^s(1) \le t^s(b') < t^s(b)\}. \end{aligned} \tag{20}$$

Define $L(a', b'; a, b)$ as a straight line with strictly positive slope joining the nodes $[t^r(a'), t^s(b')]$ and $[t^r(a), t^s(b)]$. This sets up the local optimization problem

$$\left[t^{r^*}(a'), t^{s^*}(b')\right] = \underset{(t^r(a'), t^s(b')) \in N_{\mathrm{ab}}}{\arg\min} \left(E\left(t^r(a'), t^r(a); L(a', b'; a, b)\right)\right). \tag{21}$$

Let $H(t^r(a), t^r(b))$ be the minimum cumulative cost needed to reach the point $[t^r(a), t^s(b)]$, defined as

$$\begin{aligned} H\left(t^r(a), t^s(b)\right) = \; & E\left(t^{r^*}(a'), t^r(a); L(a', b'; a, b)\right) \\ & + H\left(t^{r^*}(a'), t^{s^*}(b')\right). \end{aligned} \tag{22}$$

This minimization problem is solved sequentially for each node $[t^r(a), t^s(b)]$, starting from $[t^r(1), t^s(1)]$, and with $H(t^r(1), t^s(1)) = 0$, and increasing a and b until the node $[t^r(N_r), t^s(N_s)]$ is reached. Tracing the path created by the set of pairs $\{[t^{r^*}(1), t^{s^*}(1)], \ldots, [t^{r^*}(N_r), t^{s^*}(N_s)]\}$ provides a discrete version of the optimal continuous γ. It is important to highlight that the dynamic programming algorithm provides the exact optimal warping function for each node, i.e., the warping function found can never be a local optimum of the objective function, and, therefore, the validity of d_w and d_a will not be compromised.

In this work, we used the standard dynamic programming algorithm [26] to solve for an optimal γ in (3). It should be noted that for any fixed partition of $\boldsymbol{t}^r$, this algorithm provides the exact optimal γ that is restricted to the graph on this partition. Recently, an optimization method of performing optimization methods on Riemannian manifolds was developed [42], with one method being the Broyden-Fletcher-Goldfarb-Shanno (BFGS) algorithm. The BFGS algorithm is a faster alternative to dynamic programming. Additionally, an optimization approach using a Dirichlet prior on the warping functions, and a Markov chain Monte Carlo algorithm has been recently developed [43].

Appendix B
Mean Warped T-Wave

From a set of I T-waves, $\{\boldsymbol{f}_1^s(\boldsymbol{t}_1^s), \boldsymbol{f}_2^s(\boldsymbol{t}_2^s), \ldots, \boldsymbol{f}_I^s(\boldsymbol{t}_I^s)\}$ with temporal and amplitude variability it is possible to calculate a mean warped T-wave that is an optimal representative average both in temporal and amplitude domains. Consequently, we will iteratively search for the optimal mean warped T-wave in the SRSF domain, $\bar{\boldsymbol{q}}^k(\boldsymbol{t}^r)$, where k is the iteration, that minimizes the average of the difference between $\bar{\boldsymbol{q}}^k(\boldsymbol{t}^r)$ and each of the SRSF transformations of the set of T-waves, $\{\boldsymbol{q}_{f_1^s}(\boldsymbol{t}_1^s), \boldsymbol{q}_{f_2^s}(\boldsymbol{t}_2^s), \ldots, \boldsymbol{q}_{f_I^s}(\boldsymbol{t}_I^s)\}$. Therefore, we initialize $\bar{\boldsymbol{q}}^{k=1}(\boldsymbol{t}^r)$ as the average of $\{\boldsymbol{q}_{f_1^s}(\boldsymbol{t}_1^s), \boldsymbol{q}_{f_2^s}(\boldsymbol{t}_2^s), \ldots, \boldsymbol{q}_{f_I^s}(\boldsymbol{t}_I^s)\}$ and, then, for iteration k, we look for the optimal set of $\{\boldsymbol{\gamma}_1^{*^k}(\boldsymbol{t}^r), \boldsymbol{\gamma}_2^{*^k}(\boldsymbol{t}^r), \ldots, \boldsymbol{\gamma}_I^{*^k}(\boldsymbol{t}^r)\}$ that minimizes

$$\begin{aligned} \boldsymbol{\gamma}_i^{*^k}(\boldsymbol{t}^r) = \; & \underset{\boldsymbol{\gamma}_i(\boldsymbol{t}^r)}{\arg\min} \left(\left\|\bar{\boldsymbol{q}}^k(\boldsymbol{t}^r) - \boldsymbol{q}_{f_i^s(\boldsymbol{\gamma}_i)}(\boldsymbol{t}^r)\right\|\right). \\ & i = 1, \ldots, I. \end{aligned} \tag{23}$$

The updated SRSF transformation of the mean warped T-wave can be calculated as

$$\bar{\boldsymbol{q}}^{k+1}(\boldsymbol{t}^r) = \frac{1}{I} \sum_{i=1}^{I} \boldsymbol{q}_{[f_i^s \circ \boldsymbol{\gamma}_i^{*^k}]}(\boldsymbol{t}^r). \tag{24}$$

We repeated (23) and (24) until the difference between the energies of $\bar{\boldsymbol{q}}^{k+1}(\boldsymbol{t}^r)$ and $\bar{\boldsymbol{q}}^k(\boldsymbol{t}^r)$ was lower than 0.1%.

Then, the final mean warped T-wave can be obtained as [23], [25]

$$\bar{f}\left(t^r\left(n\right)\right)=\frac{1}{I}\sum_{i=1}^{I}f_i^s\left(t_i^s\left(1\right)\right)+\sum_{l=1}^{n}\bar{q}^k\left(t^r\left(l\right)\right)\left|\bar{q}^k\left(t^r\left(l\right)\right)\right|. \tag{25}$$

When the morphology of the set of T-waves is very homogeneous, the morphology of the mean warped T-wave will be very similar and representative of the set. However, if the morphologies in the set are heterogeneous, like when a large portion of T-waves are biphasic or S-shaped while another portion is monophasic, the mean warped T-wave morphology will resemble the dominant T-wave shape, in case there exists one, or the arithmetic T-wave mean (after warping), if the different populations have the same weight. Therefore, it would be advisable to include a preprocessing step to remove any undesired T-wave morphology prior the computation of the mean warped T-wave.

Appendix C
ECG-SIM

The transmembrane potentials, $\boldsymbol{v}(t)=[v_1(t),\ldots,v_M(t)]$, of $M=257$ sources (*nodes*), each one located at a given point on the epi- and endocardium, were generated for each node m by using the analytical expression proposed in [44], and already used for similar purposes in [45], [46]

$$\begin{aligned}
v_m\left(t\right) &= a_m\cdot\mathfrak{d}_m\left(t\right)\cdot\mathfrak{r}_m\left(t\right)+v_0, \quad m=1..M,\\
\mathfrak{d}_m\left(t\right) &= \frac{1}{1+e^{-\alpha_m\left(t-\delta_m\right)}}.\\
\mathfrak{r}_m\left(t\right) &= \left(1-\frac{1}{1+e^{-\beta_m\left(t-\rho_m\right)}}\right)\cdot\left(1-\frac{1}{1+e^{-\mu_m\left(t-\rho_m\right)}}\right).
\end{aligned} \tag{26}$$

In these expressions, δ_m and ρ_m are the depolarization and repolarization times, and α_m, β_m, and μ_m describe the upslope during repolarization, and the leading and trailing downslope during repolarization, respectively, at node m. a_m is the amplitude of the transmembrane potential and v_0 is the resting potential. The values of the parameters were obtained by fitting $v_m(t)$ with the transmembrane potential of each node provided by ECGSIM [47] for a normal male.

A L-lead ECG beat, with $L=8$, was generated by using the model proposed and validated in [33]. This model is derived from the equivalent surface source model [48], assuming that the sources are of the double layer type. The ECG potential (one for each of the L leads considered) on the body surface can be expressed as

$$\boldsymbol{\phi}\left(t\right)=\mathbf{A}\boldsymbol{v}\left(t\right) \tag{27}$$

where matrix $\mathbf{A}$ has size $(8\times M)$ and reflects the complexity of the torso (geometry and conductivity). Each row of $\mathbf{A}$ expresses the linear weighting of all action potentials, $\boldsymbol{v}(t)$, for each standard lead [33].

In [33], the author pointed out that it was possible to link the shape of the T-wave in each lead to the transmembrane potential using (27). In fact, making the further approximation that the only difference across different $v_m(t)$ functions is the repolarization time ρ_m, i.e., $v_m(t)=v(t-\rho_m)$, then the repolarization time of each node may be expressed as $\rho_m=\bar{\rho}+\Delta\rho_m$, where $\bar{\rho}=\sum_{m=1}^{M}\rho_m/M$ is the average repolarization time, and $\Delta\rho_m\ll\bar{\rho}$ is the deviation (difference) of repolarization times at cardiac site m, with standard deviation σ, from the mean repolarization time, with $\sum_{m=1}^{M}\Delta\rho_m=0$.

Acknowledgement

The authors would like to acknowledge the contribution of Dr. R. Sassi for providing the data used at the electro-physiological simulation. The computation was performed at the High Performance computing platform of the NANBIOSIS ICTS, Biomedical Research Networking Center in Bioengineering, Biomaterials and Nanomedicine (CIBER-BBN) and Aragón Institute of Engineering Research (I3A), Zaragoza, Spain.

References

[1] R. M. John *et al.*, "Ventricular arrhythmias and sudden cardiac death," *Lancet*, vol. 380, no. 9852, pp. 1520–1529, 2012.
[2] M. N. Niemeijer *et al.*, "Short-term QT variability markers for the prediction of ventricular arrhythmias and sudden cardiac death: A systematic review," *Heart*, vol. 100, no. 23, pp. 1831–1836, 2014.
[3] M. Baumert *et al.*, "QT interval variability in body surface ECG: Measurement, physiological basis, and clinical value: Position statement and consensus guidance endorsed by the European Heart Rhythm Association jointly with the ESC Working Group on Cardiac Cellular Electrophysiology," *Europace*, vol. 18, pp. 925–944, 2016.
[4] W. L. Atiga *et al.*, "Beat-to-beat repolarization lability identifies patients at risk for sudden cardiac death," *J. Cardiovascular Electrophysiol.*, vol. 9, no. 9, pp. 899–908, 1998.
[5] T. Klingenheben *et al.*, "Predictive value of T-wave alternans for arrhythmic events in patients with congestive heart failure," *Lancet*, vol. 356, no. 9230, pp. 651–652, 2000.
[6] M. P. Nash *et al.*, "Whole heart action potential duration restitution properties in cardiac patients: A combined clinical and modelling study," *Exp. Physiol.*, vol. 91, no. 2, pp. 339–354, 2006.
[7] R. Coronel *et al.*, "Dispersion of repolarization and arrhythmogenesis," *Heart Rhythm*, vol. 6, no. 4, pp. 537–543, 2009.
[8] M. J. Burgess, "Relation of ventricular repolarization to electrocardiographic T wave-form and arrhythmia vulnerability," *Amer. J. Physiol.*, vol. 236, no. 3, pp. H391–H402, 1979.
[9] W. Shimizu and C. Antzelevitch, "Cellular basis for long QT, transmural dispersion of repolarization, and torsade de pointes in the long QT syndrome," *J. Electrocardiol.*, vol. 32, no. Suppl., pp. 177–184, 1999.
[10] K. Gima and Y. Rudy, "Ionic current basis of electrocardiographic waveforms: A model study," *Circ. Res.*, vol. 90, no. 8, pp. 889–896, 2002.
[11] E. Pueyo *et al.*, "Cardiac repolarization analysis using the surface electrocardiogram," *Philos. Trans. A. Math. Phys. Eng. Sci.*, vol. 367, no. 1887, pp. 213–233, 2009.
[12] P. Laguna *et al.*, "Techniques for ventricular repolarization instability assessment for the ECG," *Proc. IEEE*, vol. 104, no. 2, pp. 392–415, Feb. 2016.
[13] A. J. Moss, "Measurement of the QT interval and the risk associated with QTc interval prolongation: A review," *Amer. J. Cardiol.*, vol. 72, no. 6, pp. B23–B25, 1993.
[14] M. S. Fuller *et al.*, "Estimates of repolarization dispersion from electrocardiographic measurements," *Circulation*, vol. 102, no. 6, pp. 685–691, 2000.
[15] W. Zareba *et al.*, "Automatic detection of spatial and dynamic heterogeneity of repolarization," *J. Electrocardiol.*, vol. 27, no. Suppl., pp. 66–72, 1994.
[16] A. Mincholé *et al.*, "Quantification of restitution dispersion from the dynamic changes of the T-wave peak to end, measured at the surface ECG," *IEEE Trans. Biomed. Eng.*, vol. 58, no. 5, pp. 1172–1182, May 2011

[17] S. M. Narayan, "T-wave alternans and the susceptibility to ventricular arrhythmias," *J. Am. Coll. Cardiol.*, vol. 47, no. 2, pp. 269–281, 2006.
[18] P. Brugada and J. Brugada, "Right bundle branch block, persistent ST segment elevation and sudden cardiac death: A distinct clinical and electrocardiographic syndrome: A multicenter report," *J. Amer. Coll. Cardiol.*, vol. 20, no. 6, pp. 1391–1396, 1992.
[19] B. Acar *et al.*, "Spatial, temporal and wavefront direction characteristics of 12-lead T-wave morphology," *Med. Biol. Eng. Comput.*, vol. 37, no. 5, pp. 574–584, 1999.
[20] D. Cuesta-Frau *et al.*, "Enhanced modified moving average analysis of T-wave alternans using a curve matching method: A simulation study," *Med. Biol. Eng. Comput.*, vol. 47, no. 3, pp. 323–331, 2009.
[21] M. Kotas, "Projective filtering of time warped ECG beats," *Comput. Biol. Med.*, vol. 38, no. 1, pp. 127–137, 2008.
[22] M. Schmidt *et al.*, "Two-dimensional warping for one-dimensional signals: conceptual framework and application to ECG processing," *IEEE Trans Signal Process*, vol. 62, no. 21, pp. 5577–5588, Sep. 2014
[23] A. Srivastava *et al.* "Registration of functional data using fisher-rao metric," arXiv preprint arXiv:1103.3817, 2011.
[24] J. O. Ramsay and X. Li, "Curve registration," *J. R. Statist. Soc. Series B Statist. Methodology*, vol. 60, no. 2, pp. 351–363, 1998.
[25] J. D. Tucker *et al.*, "Generative models for functional data using phase and amplitude separation," *Comput. Statist. Data Anal.*, vol. 61, pp. 50–66, 2013.
[26] D. P. Bertsekas, *Dynamic Programming and Optimal Control*. Belmont, MA, USA: Athena Scientific, 1995, vol. 1, no. 2.
[27] A. Srivastava *et al.*, "Shape analysis of elastic curves in euclidean spaces," *IEEE Trans. Pattern Anal. Mach. Intell.*, vol. 33, no. 7, pp. 1415–1428, Oct. 2010.
[28] P. W. Holland and R. E. Welsch, "Robust regression using iteratively reweighted least-squares," *Commun. Statist. Theory Methods*, vol. 6, no. 9, pp. 813–827, 1977.
[29] P. Laguna *et al.*, "Automatic detection of wave boundaries in multilead ECG signals: Validation with the CSE database," *Comput. Biomed. Res.*, vol. 27, no. 1, pp. 45–60, 1994.
[30] F. Castells *et al.*, "Principal component analysis in ECG signal processing," *EURASIP J. Appl. Signal Process.*, vol. 2007, no. 1, pp. 98–98, 2007.
[31] J. P. Martínez *et al.*, "A wavelet-based ECG delineator: Evaluation on standard databases," *IEEE Trans. Biomed. Eng.*, vol. 51, no. 4, pp. 570–581, Apr. 2004.
[32] Task force of the European Society of Cardiology and the North American Society of Pacing and Electrophysiology,"Heart rate variability standards of measurement, physiological interpretation, and clinical use," *Eur. Heart. J.*, vol. 17, pp. 354–381, 1996.
[33] A. van Oosterom, "Genesis of the T wave as based on an equivalent surface source model," *J. Electrocardiol.*, vol. 34, no. Suppl, pp. 217–227, 2001.
[34] E. Gil *et al.*, "Photoplethysmography pulse rate variability as a surrogate measurement of heart rate variability during non-stationary conditions," *Physiol. Meas.*, vol. 31, no. 9, pp. 1271–1290, 2010.
[35] D. C. Howell, "Median absolute deviation," in *Wiley StatsRef: Stat Ref Online*. Hoboken, NJ, USA: Wiley, 2005.
[36] J. Ramírez *et al.*, "Automatic SVM classification of sudden cardiac death and pump failure death from autonomic and repolarization ECG markers," *J. Electrocardiol.*, vol. 48, no. 4, pp. 551–557, 2015.
[37] R. D. Berger, "Methodology for automated QT variability measurement," U.S. Patent 08/340, 861, Oct. 1st, 1996.
[38] G. Piccirillo *et al.*, "QT variability strongly predicts sudden cardiac death in asymptomatic subjects with mild or moderate left ventricular systolic dysfunction: A prospective study," *Eur. Heart J.*, vol. 28, no. 11, pp. 1344–1350, 2007.
[39] R. D. Berger *et al.*, "Beat-to-beat QT interval variability: Novel evidence for repolarization lability in ischemic and nonischemic dilated cardiomyopathy," *Circulation*, vol. 96, no. 5, pp. 1557–1565, 1997.
[40] H. J. L. M. Vullings *et al.*, "ECG segmentation using time-warping," in *Proc. Int. Symp. Intell. Data Anal.*, 2006, 275–285.
[41] A. Zifan *et al.*, "Automated segmentation of ECG signals using piecewise derivative dynamic time warping," *Int. J. Biol. Life Sci.*, vol. 1, pp. 181–185, 2007.
[42] W. Huang *et al.*, "A broyden class of Quasi-Newton methods for riemannian optimization," *SIAM J. Optim.*, vol. 25, no. 3, pp. 1660–1685, 2015.
[43] W. Cheng *et al.*, "Bayesian registration of functions and curves," *Bayesian Anal.*, vol. 11, no. 2, pp. 447–475, 2016.
[44] P. van Dam *et al.*, "Non-invasive imaging of cardiac activation and recovery," *Ann. Biomed. Eng.*, vol. 37, no. 9, pp. 1739–1756, 2009.
[45] R. Sassi and L. T. Mainardi, "An estimate of the dispersion of repolarization times based on a biophysical model of the ECG," *IEEE Trans. Biomed. Eng.*, vol. 58, no. 12, pp. 3396–3405, Dec. 2011.
[46] M. Orini *et al.*,"Detection of transient, regional cardiac repolarization alternans by time-frequency analysis of synthetic electrograms," in *Proc. Conf. IEEE Eng. Med. Biol. Soc.*, pp. 3773–3776, 2013.
[47] A. van Oosterom and T. F. Oosterndorp, "ECGSIM: An interactive tool for studying the genesis of QRST waveforms," *Heart*, vol. 90, no. 2, pp. 165–168, 2004.
[48] D. B. Geselowitz, "Description of cardiac sources in anisotropic cardiac muscle. Application of bidomain model," *J. Electrocardiol.*, vol. 25, no. Suppl., pp. 65–67, 1992.

Julia Ramírez received the M.S. degree in telecommunications engineering and the M.S. degree in biomedical engineering from the University of Zaragoza, Zaragoza, Spain, in 2011 and 2013, respectively. She is currently working toward the Ph.D. degree at the University of Zaragoza, Zaragoza, Spain.

Her current research interest focuses on biomedical signal processing, especially in the search for arrhythmic risk markers from the electrocardiogram signal.

Michele Orini received the M.S. degree in biomedical engineering from the Politecnico di Milano, Milano, Italy, the engineering degree from the École Céntrale Paris, Châtenay-Malabry, France, and the Ph.D. degree in biomedical engineering from the University of Zaragoza, Zaragoza, Spain and the Politecnico di Milano.

He is currently a Research Fellow at the University College London and Barts Heart Centre, St. Bartholomew's Hospital, London, U.K. His current research interest focuses on the study of cardiac arrhythmia mechanisms.

J. Derek Tucker received the B.S. and M.S. degrees in electrical engineering from Colorado State University, Fort Collins, CO, USA, in 2007 and 2009, respectively, and the Ph.D. degree in statistics from Florida State University, Tallahassee, FL, USA, in 2014.

He is currently a Senior member of the technical staff at Sandia National Laboratories in Albuquerque, NM, USA. His current research interest focuses on statistical image understanding with a focus on object classification.

Esther Pueyo received the M.S. degree in mathematics and the Ph.D. degree in biomedical engineering from the University of Zaragoza, Zaragoza, Spain, in 1999 and 2006, respectively.

She is currently an Associate Professor at the University of Zaragoza. Her current research interest focuses on the mechanisms and manifestations of cardiac arrhythmias at scales ranging from cellular ion channels to the electrocardiogram.

Pablo Laguna received the M.S. degree in physics and the Ph.D. degree in physics, specialization in signal processing, from the University of Zaragoza, Zaragoza, Spain, in 1985 and 1990, respectively.

He is currently a Full Professor at the University of Zaragoza. He has co-authored more than 200 research papers. His current research interest focuses on signal processing, in particular with biomedical applications.